Unveiling Liquid-Crystalline Lipids in the Urothelial Membrane through Cryo-EM

Authors: Haruaki Yanagisawa[1], Yoshihiro Kita[2,3], Toshiyuki Oda[4*], and Masahide Kikkawa[1*]

Affiliations:

[1] Department of Cell Biology and Anatomy, Graduate School of Medicine, The University of Tokyo, 7-3-1 Hongo, Bunkyo-ku, Tokyo, 113-0033, Japan,

[2] Life Sciences Core Facility, Graduate School of Medicine, The University of Tokyo, 7-3-1 Hongo, Bunkyo-ku, Tokyo 113-0033, Japan,

[3] Department of Lipidomics, Graduate School of Medicine, The University of Tokyo, 7-3-1 Hongo, Bunkyo-ku, Tokyo 113-0033, Japan.

[4] Department of Anatomy and Structural Biology, Graduate School of Medicine, University of Yamanashi, 1110 Shimokato, Chuo, Yamanashi, 409-3898, Japan.

*Correspondence to: toda@yamanashi.ac.jp, mkikkawa@m.u-tokyo.ac.jp

Abstract

The urothelium, a distinct epithelial tissue lining the urinary tract, serves as an essential component in preserving urinary tract integrity and thwarting infections. The asymmetric unit membrane (AUM), primarily composed of the uroplakin complex, constitutes a critical permeability barrier in fulfilling this role. However, the molecular architectures of both the AUM and the uroplakin complex have remained enigmatic due to the paucity of high-resolution structural data. In this investigation, we employed cryo-electron microscopy to elucidate the three-dimensional structure of the uroplakin complex embedded within the porcine AUM at a resolution of 3.5 Å. Our findings unveiled that the uroplakin complexes are situated within hexagonally arranged crystalline lipid membrane domains, rich in hexosylceramides. Moreover, our research rectifies a misconception in a previous model by confirming the existence of a domain initially believed to be absent, and pinpointing the accurate location of a crucial Escherichia coli binding site implicated in urinary tract infections. These discoveries offer valuable insights into the molecular underpinnings governing the permeability barrier function of the urothelium and the orchestrated lipid phase formation within the plasma membrane.

Introduction

The urothelium, which lines the urinary tract, performs a dual function: it serves as a permeability barrier, effectively preventing the leakage of urine components into surrounding tissue while undergoing morphological changes to adapt to the distention and contraction that occurs during the micturition cycle (Deng et al., 2001; Wu et al., 2009; Apodaca, 2004; Khandelwal et al., 2009). The apical surface of the urothelium is covered by numerous structurally rigid membrane plaques, known as asymmetric unit membranes (AUM), as observed by electron microscopy (Hicks, 1965; Hu et al., 2000; Jenkins and Woolf, 2007). The AUMs are composed of hexagonally arranged 16-nm uroplakin complexes containing four major proteins, UPIa, UPIb, UPII, and UPIIIa (Lee, 2011). UPIa and UPIb have four transmembrane domains and belong to the tetraspanin family (Yu et al., 1994). Meanwhile, UPII and UPIIIa each possess a single transmembrane domain and form Ia/II and Ib/IIIa heterodimers within the endoplasmic reticulum (ER) in conjunction with UPIa and UPIb, respectively (Hu et al., 2005; Tu et al., 2002). In the post-Golgi compartment, UP heterodimers are assembled into paracrystalline arrays (Liang et al., 2001). The AUM's quasi-crystalline symmetry has been leveraged in the structural investigation of the uroplakin complex, as documented by several studies (Min et al., 2006; Min et al., 2003; Min et al., 2002; Walz et al., 1995; Zhou et al., 2001). While cryo-electron microscopy of tannic-acid-stained AUM has enabled the identification of the orientation of transmembrane helices in tetraspanin pairs (Min et al., 2006; Wang et al., 2009), the resolution of the resulting electron density map remains insufficient for a comprehensive study of the secondary structures of the extracellular domains or for the localization of individual UP subunits.

The uroplakin complex also plays a crucial role in the development of urinary tract infections, as it facilitates *Escherichia coli's* attachment to the urothelium (Hultgren et al., 1993; Hooton and Stamm, 1997). This attachment is facilitated by the interaction between the N-

glycosylated UPIa's mannose residues and the FimH lectin located at the tip of the bacterium's pili (Zhou et al., 2001). The binding of FimH to UPIa triggers phosphorylation of UPIIIa and subsequent apoptosis of the urothelial cells (Thumbikat et al., 2009). Furthermore, it has been postulated that this FimH-UPIa interaction induces conformational alterations in the transmembrane helix bundles (Wang et al., 2009). However, it is unclear whether FimH's binding to a flexible carbohydrate chain can change the conformation of a rigid uroplakin complex. In addition, the positioning of the heterodimer has been inferred by comparing the uroplakin structure with and without bound FimH [Min G, 2002]. Nevertheless, the low resolution of the electron density map hinders the validity of these conclusions.

In this study, we reconstructed the 3D structure of the uroplakin complex by observing tilted AUMs using cryo-electron microscopy. By combining random conical tilt and single particle analysis (Sorzano et al., 2015; Frank et al., 1978; Righetto et al., 2019; Radermacher, 1988), we were able to build an accurate model of the uroplakin hexameric complex.

Results

Cryo-Electron Microscopy of AUM

To determine the high-resolution structure of the uroplakin complex, we isolated the AUM from porcine urinary bladders, leveraging its resistance to sarkosyl (Liang et al., 1999), and employed cryo-electron microscopy techniques. Initially, we used cryo-electron tomography to observe the AUM; however, the obtained structure was of low resolution as a result of the irradiation-induced distortion of the specimen (Oda et al., 2022; Dutka et al., 2023). Subsequently, we performed single particle analysis on AUM samples tilted up to 55° (Figures 1A and 1B), resulting in a global resolution of 3.5 Å, with 3.2 Å and 6.2 Å resolutions in the transverse and vertical directions, respectively (Figures 1C, 1D, and S1B).

These resolutions allowed us to construct a model of the main chains and some side chains, based on AlphaFold predictions, with the exceptions of the 90-101 loop of UPII and the cytoplasmic loop of UPIIIa due to their flexibility (Jumper et al., 2021) (Figure 2).

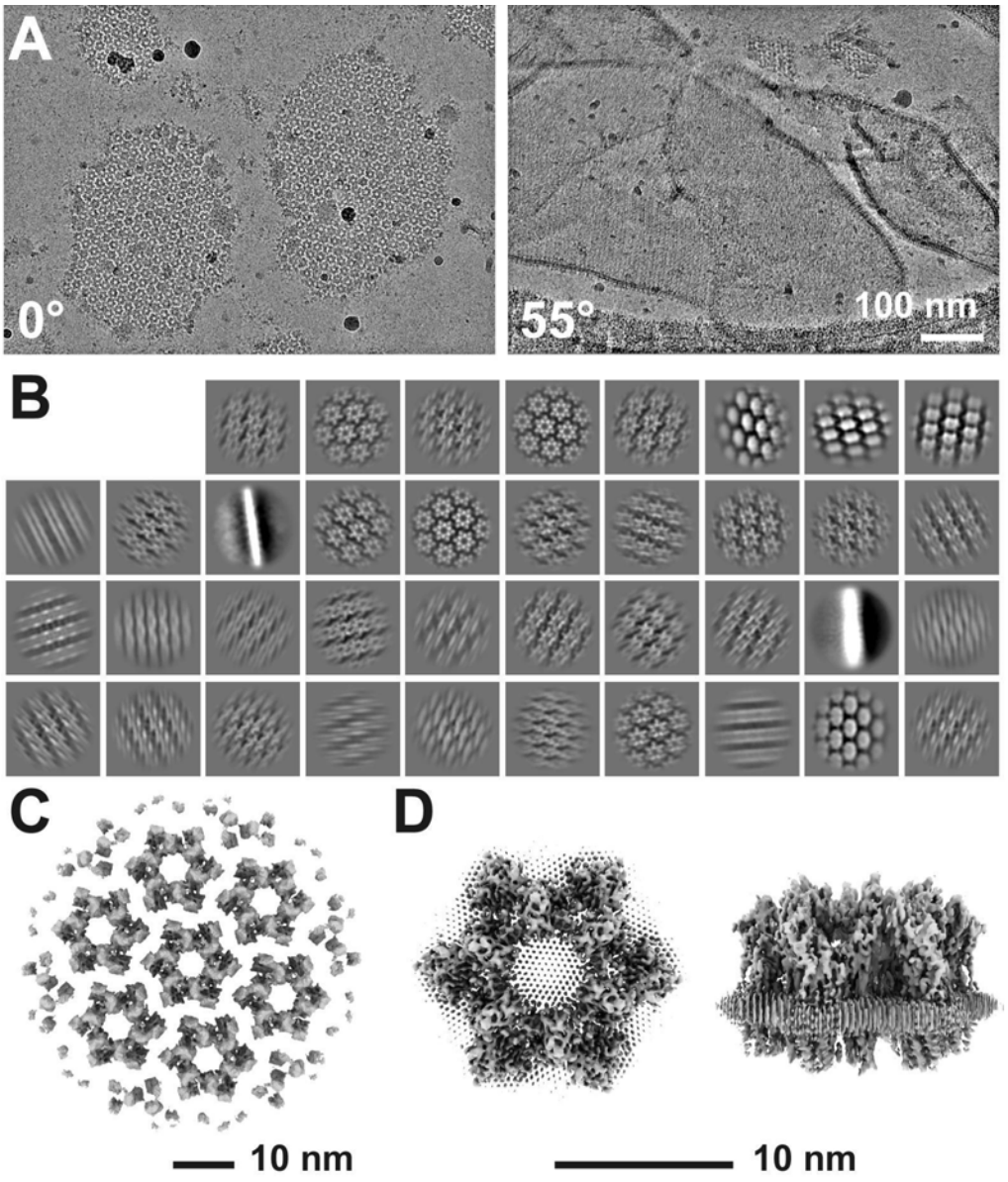

Figure 1

To our surprise, we found that the hexagonally arranged liquid-crystalline lipids were not only within the central pore but also in the inter-complex regions, spanning the entire outer leaflet of the AUM (Figure 1D, 2A). The crystalline lipids were tightly packed, with a

distance of ~4.8 Å between them (Zhao et al., 2021; Ghysels et al., 2019). Further local refinement focusing on the extracellular domain revealed the additional outermost part of the lipid densities, suggesting a structural heterogeneity in the association between the lipids and the uroplakin complex (Figure S1A). Although the head groups of most lipids were unresolved due to the insufficient vertical resolution and the random orientations, densities of some lipids were continuous with those of the side chains, suggesting possible interactions (Figure 2C). Some lipids appeared to be stabilized by vertically-aligned bulky side chains (Figure 3) (Ulmschneider and Sansom, 2001). Although the majority of ordered sphingolipids are typically found in the outer leaflet of the plasma membrane (Simons and Ehehalt, 2002; Kusumi et al., 2020), weak signals of inner leaflet lipids were detected between the UPIa and Ib transmembrane domains (Figure S2A). The presence of hexagonally-aligned lipids in the inner leaflet possibly contributes to the AUM's exceptional rigidity. These crystalline lipids in the AUM are likely to play an essential role in the barrier function of the urothelium (see Discussions).

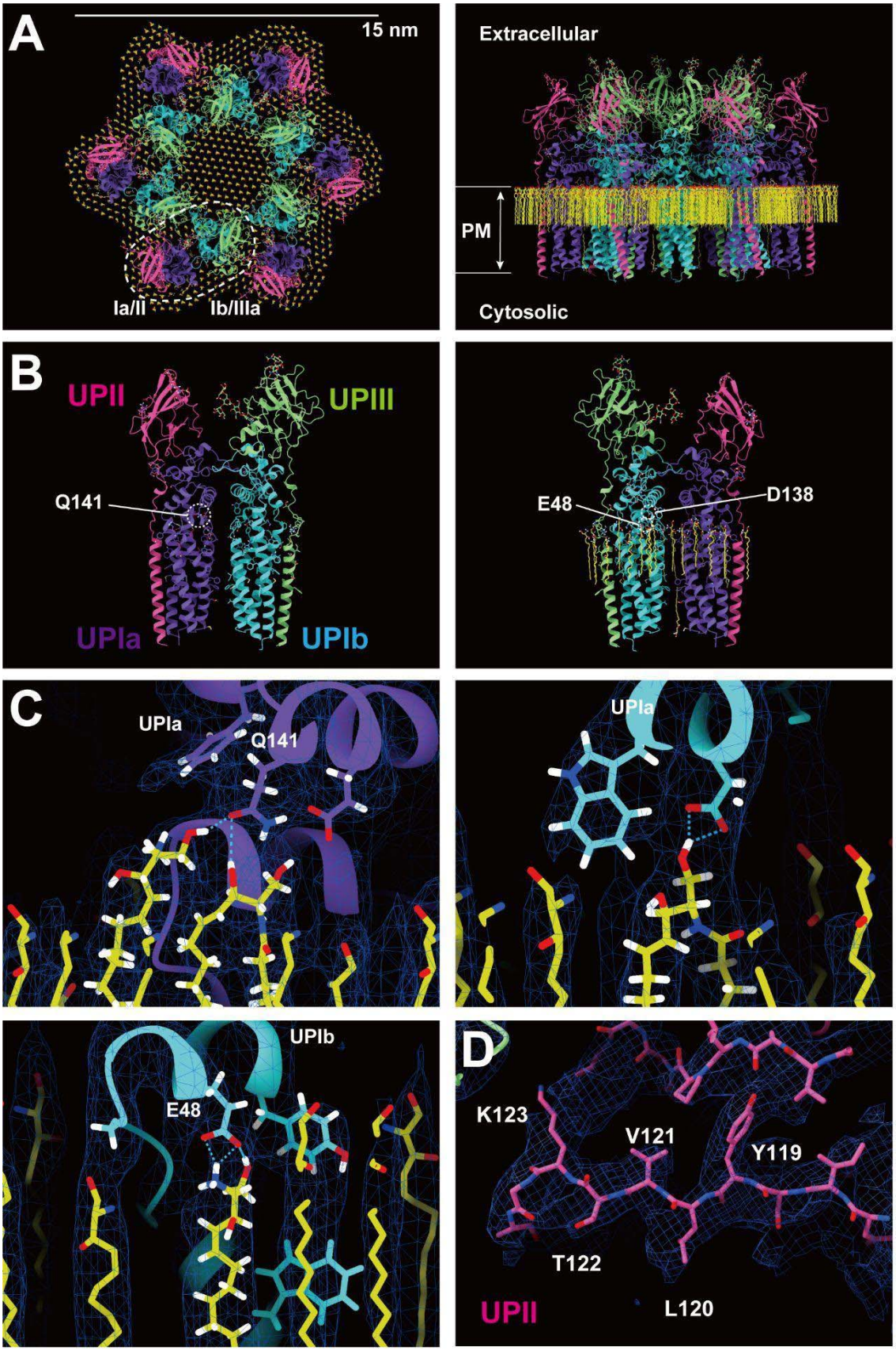
A
15 nm
Ia/II
Ib/IIIa
Extracellular
PM
Cytosolic
B
UPII
UPIII
Q141
UPIa
UPIb
E48
D138
C
UPIa
Q141
UPIa
UPIb
E48
D
K123
V121
Y119
T122
UPII
L120

Figure 2

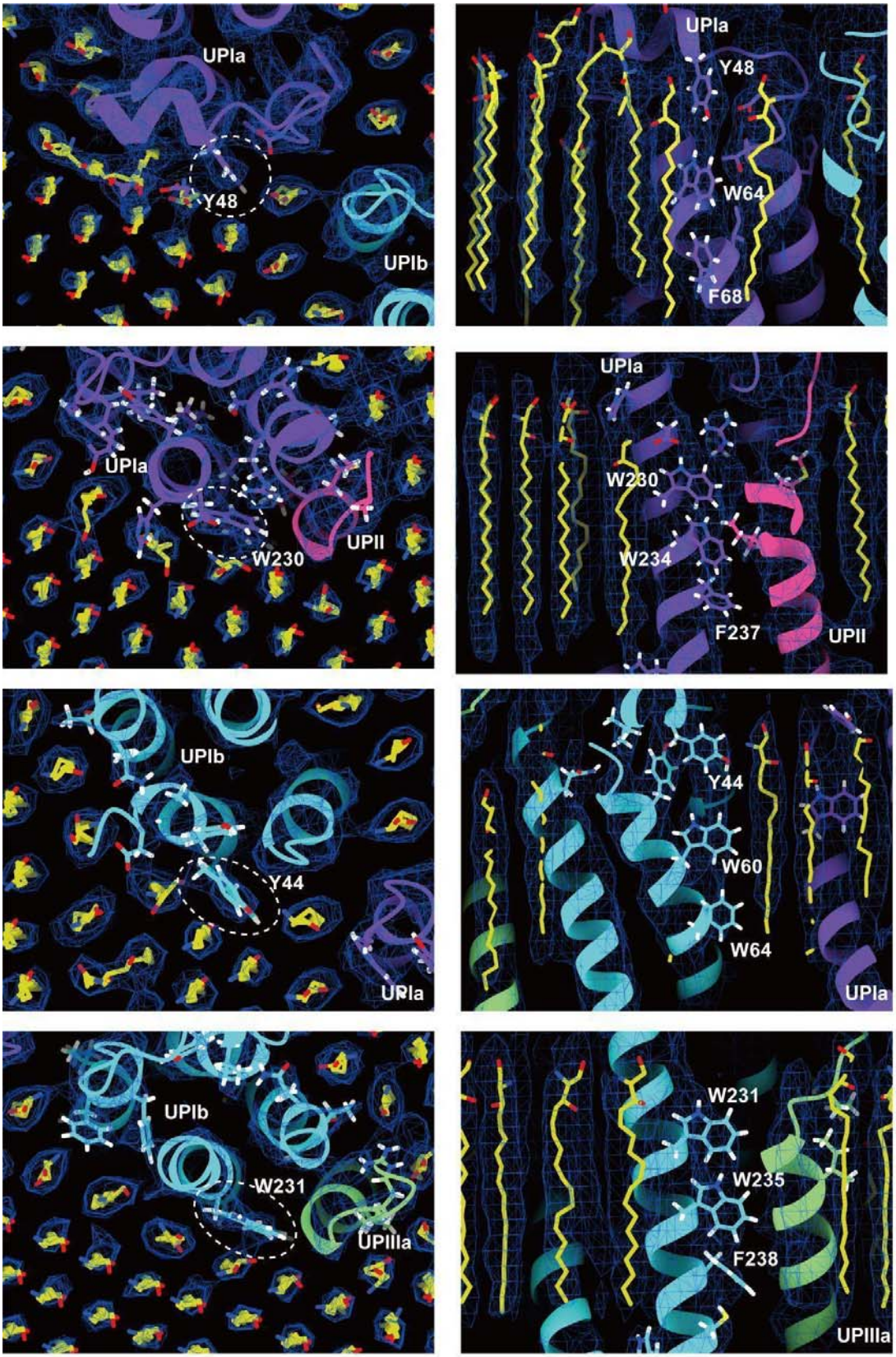
UPIa
Y48
UPIb
UPIa
Y48
W64
F68
UPIa
W230
UPII
UPIa
W230
W234
F237
UPII
UPIb
Y44
UPIa
Y44
W60
W64
UPIa
UPIb
W231
UPIIIa
W231
W235
F238
UPIIIa

Figure 3

Subunit arrangement of the uroplakin complex

The cryoEM structure of the uroplakin complex reveals that the extracellular domains of both UPII and UPIIIa exhibit distinctive beta-sheet structures (Figure 2A, B, D), which could have functional implications in protein binding or adhesion of pathogens. With these extracellular domains of UPII and UPIIIa, uroplakin heterotetramer overall adopts a Y-shaped conformation, which creates a substantial groove that may also provide a binding interface for other proteins (Figure S2A, white arrow). Adjacent heterotetramers are connected through arches formed by the UPII and UPIIIa extracellular domains. Interestingly, beneath these arches, a channel is present, which is continuous with the central cavity space (Figure S2A, red arrows). The biochemical robustness of the uroplakin hexameric complex, despite its abundance of inner cavities, can likely be attributed to the reinforcement provided by the lipid domains.

The prevailing hypothesis concerning the subunit arrangement of the uroplakin complex suggests that Ia/II and Ib/IIIa heterodimers form the inner and outer subdomains, as inferred from electron microscopy studies of FimH-bound AUM (Zhou et al., 2001; Min et al., 2002). However, our high-resolution reconstruction revealed that Ia/II and Ib/IIIa heterodimers constitute the outer and inner subdomains, respectively (Figure 2A). Additionally, it has been reported that the cleavage of UPII at Arg84 by furin results in the removal of the N-terminal pro-sequence (amino acids 25-84) from the uroplakin complex (Lin et al., 1994; Hu et al., 2005). However, our findings suggest that the prosequence forms the external surface of the complex through the formation of several beta sheets (Figure S2B). Moreover, our reconstruction uncovered the presence of carbohydrate chains on six N-glycosylated residues, namely UPIa Asn169, UPIb Asn131, UPII Asn28, Asn57, UPIIIa Asn139, and Asn170 in accordance with previous studies (Figure 4) (Hu et al., 2005; Kanik-Prastowska et al., 2014; Wu et al., 1995). Previous electron microscopy studies have suggested that UPIa Asn169,

functioning as the binding site for the bacterial FimH protein, is located at the apex of the inner subdomain (Min et al., 2002; Xie et al., 2006). However, our reconstruction placed this glycosylated residue on the external surface of the uroplakin complex. Our structural analysis of the FimH-bound uroplakin complex also supports this assignment, as it demonstrates a weak additional density in the vicinity of Asn169 of UPIa (Figure S3A). Although a previous cryo-electron microscopy study of tannic-acid-stained uroplakin complexes reported alterations in the transmembrane helices (Wang et al., 2009), our analysis of the FimH-bound uroplakin structure did not detect any discernible conformational changes (Figure S3A) (see Discussion).

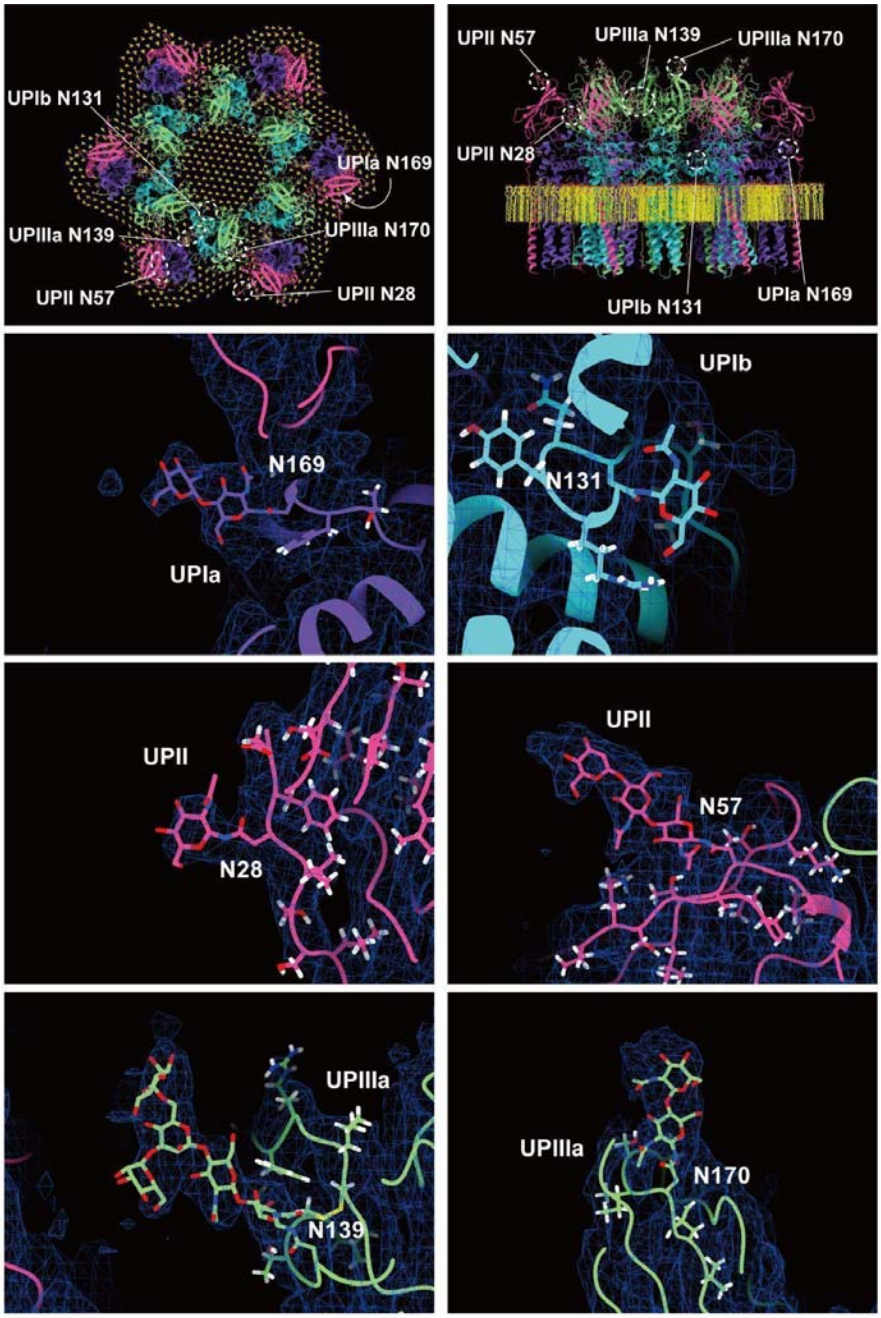

Figure 4

Inter-subunit interactions within the uroplakin complex

Our map and model suggest that the hexameric complex is assembled through three inter-subunit interfaces: the Ia-Ib, II-IIIa, and IIIa-IIIa interfaces. The Ia-Ib interface appears similar to that reported in the PRPH2-ROM1 tetraspanin complex (Figure 5A) (El and Gros,

2022). The interface is stabilized by various interactions, including a hydrophobic interaction between Phe196 of UPIa and Leu155 of UPIb (Figure 5B), and a hydrogen bond between Asn195 of UPIa and Gln130 of UPIb (Figures 5C and 5D).

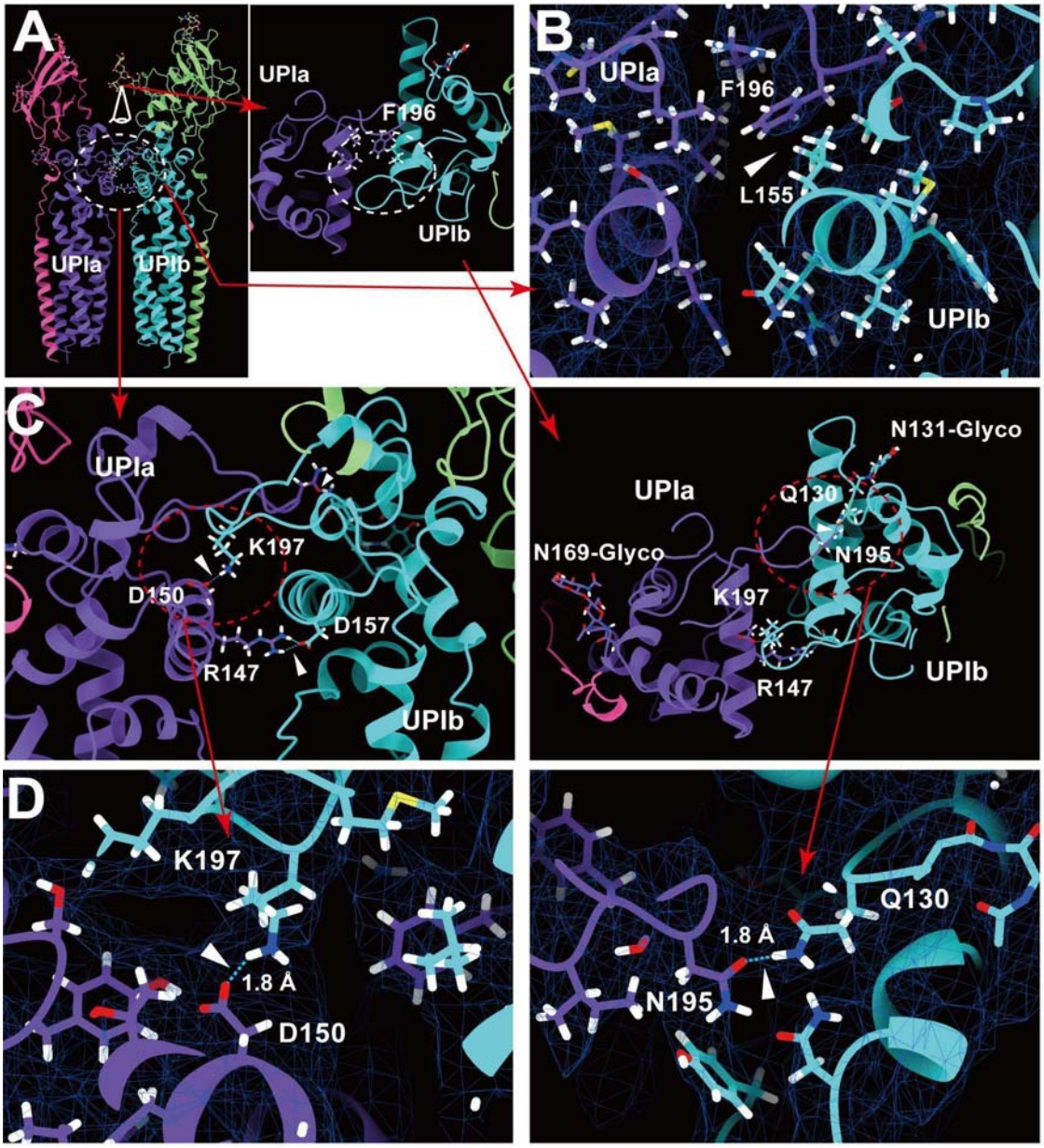

Figure 5

The resolution of the II-IIIa interface, particularly near the flexible loop 90-101 of UPII, is of lower quality. However, it appears to be stabilized by a hydrophobic cluster of a disulfide bond between Cys51-80 and Pro79 of UPII, a disulfide bond between Cys47-Cys110, and

Leu113 of UPIIIa (Figure 6A).

Finally, the UPIIIa extends its loop 137-161 into the groove of an adjacent IIIa, forming an interface stabilized by a hydrophobic cluster composed of Pro146 of IIIa, Leu66, and Trp182 of the adjacent IIIa (Figures 6B). Additionally, a hydrophobic cluster between the transmembrane helices of UPIa and Ib appears to stabilize the heterotetramer (Figure 6C). These multiple interactions are thought to contribute to the highly rigid nature of the uroplakin complex and the AUM.

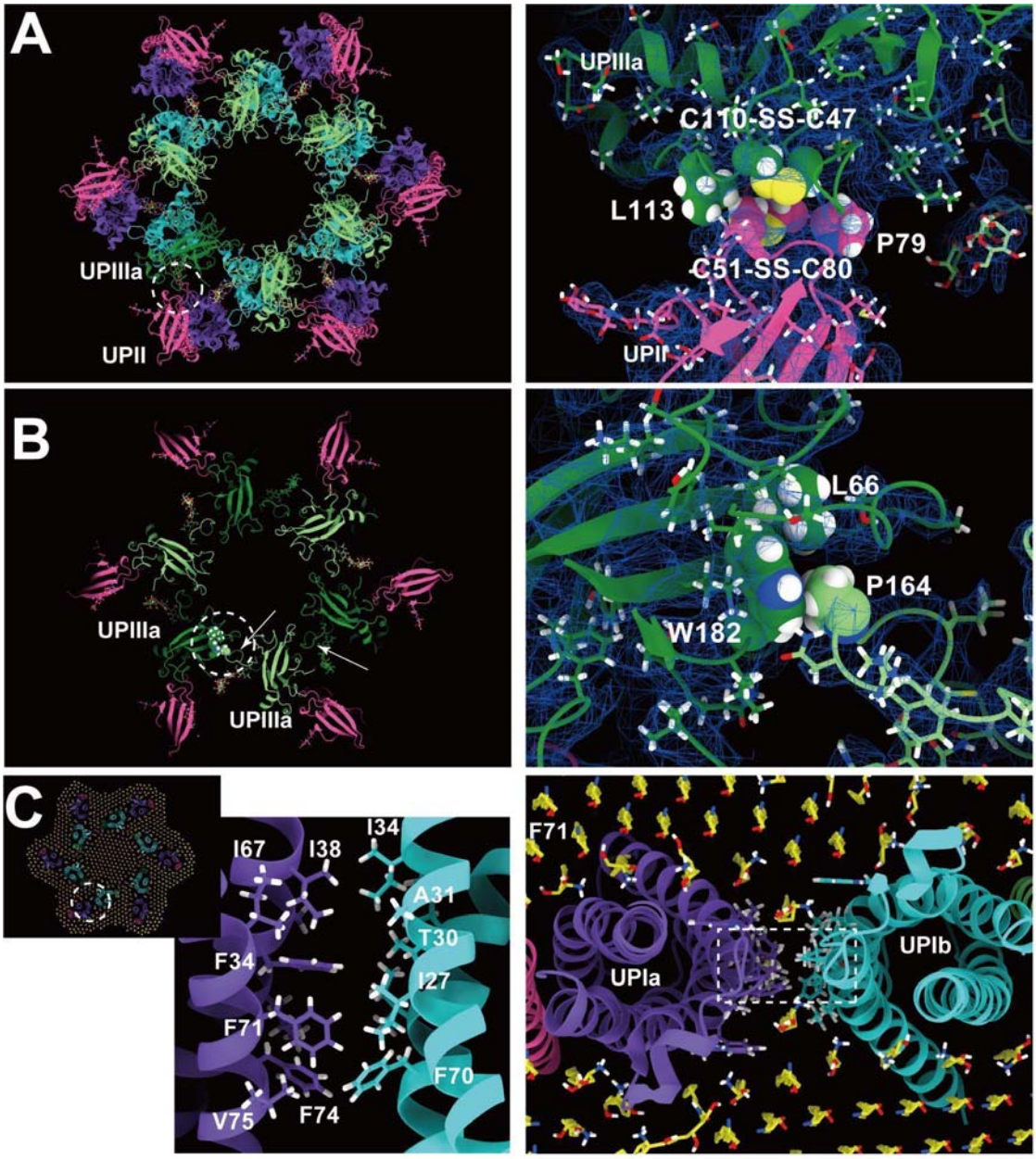

Figure 6

Lipidomic analysis of the AUM

A lipidomic analysis was conducted to discern the lipid species comprising the characteristic paracrystalline array of the AUM. The lipid composition of the sarkosyl-insoluble fraction, primarily consisting of the AUM, was compared to that of the total urothelial membrane homogenates (Figure 7 and Supplemental spread sheet 1). The results, as depicted by the LC-MS profile, revealed the enrichment of hexosylceramides in the AUM, in accordance with the

previous studies (Hicks et al., 1974; Stubbs et al., 1979; Watanabe et al., 2022). We also observed enrichment of ceramides, which is likely to be fragmentation products of ionization. These results suggest that the hexagonally-arranged lipid domain is composed of hexosylceramides.

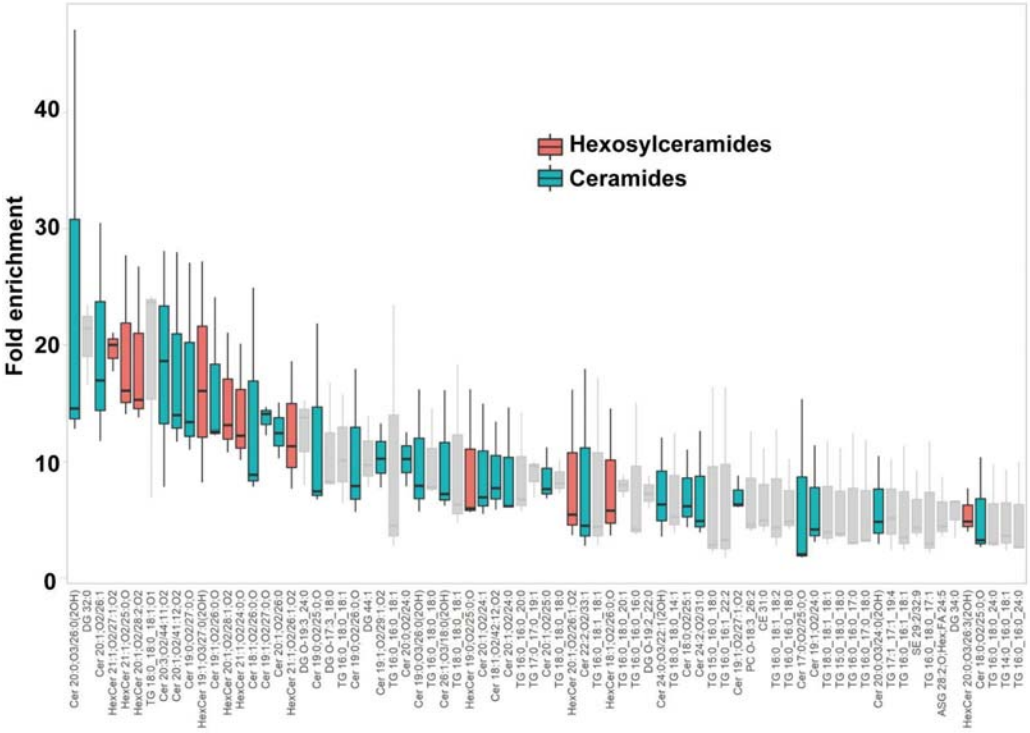

Figure 7

Discussion

The structures of the AUM and the uroplakin have been extensively analyzed utilizing electron microscopy (Min et al., 2006; Min et al., 2003; Min et al., 2002; Walz et al., 1995; Zhou et al., 2001). One of the studies achieved a resolution of approximately 6 Å in the membrane plane, yet the vertical resolution was limited to 12.5 Å, thus failing to uncover the residue-level information (Min et al., 2006). This limited structural information led to incorrect subunit assignment of the uroplakin (Min et al., 2002). The Ia/II heterodimer has long been believed to form the inner subdomain of the uroplakin hexameric complex based on the observation of additional densities in the difference map between the uroplakin

structures with and without bound FimH, which interacts with glycosylated UPIa (Zhou et al., 2001). However, our reconstruction revealed that these “additional densities” are likely artifacts of the low-resolution EM maps, as the Ia/II heterodimer actually constitutes the outer subdomain of the uroplakin (Figure 2A and S2B). Reports indicate that FimH binding to UPIa induces conformational changes in the uroplakin’s transmembrane domains (Wang et al., 2009). We also solved the structure of FimH-bound uroplakin, but no structural changes were observed (Figure S3A). The high flexibility of the carbohydrate chain and the fast on/off rate of FimH-mannose binding make it challenging to visualize the attached FimH and the induced conformational changes, if any (Lee et al., 2015; Prestegard, 2021; Sauer et al., 2016). Although the structure of the FimH-bound uroplakin complex remained unchanged compared with the unbound state, the difference map indicated an alteration in the signal intensities of crystalline lipids near the Ia/II heterodimer (Figure S3A, middle). This result suggests that FimH-binding changes the fluidity or the organization of the crystalline lipid membrane, which can initiate signal transduction (Desai and Miller, 2018; Los and Murata, 2004). Given that FimH molecules appear to fit in the space between the two adjacent uroplakin complexes (Figure S3B), the resulting molecular packing/crowding of FimH-bound uroplakin complexes could apply tension to the AUM, leading to cellular responses (Balogh et al., 2005; Zhang et al., 2021). The precise mechanism by which the attachment of FimH to the flexible carbohydrate chain induces intracellular signal remains to be determined (Thumbikat et al., 2009).

Intriguingly, the prosequence of UPII persists within the mature uroplakin complex. The precursor form of UPII, which has a molecular weight of 29 kDa, is cleaved by the enzyme furin in the trans-Golgi network. This results in the separation of the N-terminal glycosylated prosequence and the “mature” UPII, which lacks glycosylation and has a molecular weight of

15 kDa (Lin et al., 1994; Hu et al., 2005; Kanik-Prastowska et al., 2014). However, it has been documented that the S2' fragment of SARS-CoV-2 spike protein remains associated with the molecule after cleavage by furin (Ord et al., 2020; Johnson et al., 2021). This observation holds true for the UPII prosequence. The question arises as to why only a single UPII band was observed in the electrophoresis of the AUM. One potential explanation is that the estimated molecular weight of the glycosylated UPII prosequence is roughly 14 kDa, and thus it may align with the 15 kDa band. Another possibility is that the heterogeneous nature of the glycosylation chains, which make up over half of the prosequence's mass, may not produce a distinguishable band in the electrophoresis.

The epithelial lining of the bladder demonstrates a distinct impermeability to water, protons, and urea, effectively preventing the infiltration of urinary substances into the surrounding tissue (Negrete et al., 1996; Lavelle et al., 1998). Depletion of uroplakin complexes from the urothelial apical membrane by UPIII knockout leads to a two-fold increase in water permeability. Yet, the urothelial barrier maintains a substantial degree of resistance to water and urea permeation (Hu et al., 2002). These observations imply that the lipids and the uroplakin exert complementary influences on the barrier properties of the urothelial apical membrane. Our lipidomic analysis revealed an enrichment of hexosylceramide in the AUM (Figure 7) (Stubbs et al., 1979). Previous studies have established that ceramides tend to associate with each other, and an accumulation of these molecules can form a liquid crystalline phase (Huang et al., 1996; Ghysels et al., 2019). The formation of ceramide-enriched crystalline lipid domains has also been linked to the clustering of CD95 (Grassme et al., 2001; Grassme et al., 2001). These findings suggest that the accumulation of hexosylceramides in the AUM may play a role in the formation of a hexagonal lattice structure of uroplakin (Min et al., 2003).

Molecular dynamics simulations have predicted that sphingolipids form hexagonally arranged liquid-ordered phases (Sodt et al., 2015; Ghysels et al., 2019). The yeast plasma membrane H+-ATPase, Pma1 hexamer, has been demonstrated to encircle a liquid-crystalline membrane microdomain (Zhao et al., 2021). Our findings represent the first direct visualization of hexagonally organized liquid crystalline membrane domains in mammalian cells. Although the liquid-ordered phase of the lipid domain is believed to be essentially impermeable to water and ions, small molecules can traverse the membrane at the boundary between ordered and disordered domains (Ghysels et al., 2019; Gensure et al., 2006). It is noteworthy that the uroplakin-free hinge regions that connect the neighboring AUM plaques also exhibit resistance to sarkosyl and alkali treatments, indicating highly specialized structures (Liang et al., 1999). These hinge regions may serve to prevent the penetration of small molecules at the boundary between the plaques.

While our team was successful in constructing a model of the uroplakin complex, we encountered a limitation in the resolution of the vertical dimension, which hindered our ability to confidently determine the precise positioning of the side chains. To overcome this challenge, we propose the utilization of high-resolution subtomogram averaging, as it has the capability to bypass the overlap of molecules in the high-tilt views. However, to effectively implement this technique, it is imperative to devise an advanced algorithm that can accurately rectify the significant deformation of the AUM caused by irradiation.

Methods

Isolation of porcine AUM

Fresh porcine bladders were obtained from a local slaughterhouse. The AUM was isolated according to the previous study with modifications (Liang et al., 1999). The urothelium was

scraped from the luminal surface with a medicine scoop and suspended in ice-cold PBS. After centrifugation at 1,500 ×g at 4 ℃ for 5 minutes, the pellets were homogenized with a Dounce glass homogenizer in buffer A (10 mM Hepes, pH 7.4, 1 mM EDTA, and protease inhibitor cocktail). After centrifugation at 2,500 × g at 4 ℃ for 10 minutes, the pellets were resuspended in buffer A, loaded onto a 1.6 M sucrose cushion, and centrifuged at 46,000 ×g at 4 ℃ for 30 minutes. The membrane fraction concentrated at the interface was collected, loaded onto a 1.6 M sucrose cushion, and centrifuged once again. The collected membrane fraction was resuspended in buffer A plus 2% sarkosyl and incubated at room temperature for 10 minutes. Sarkosyl-insoluble membranes were collected after centrifugation at 18,000 ×g at 4 °C for 30 minutes. The pellets were further washed by resuspension in 25 mM NaOH, and centrifuged at 18,000 ×g at 4 ℃ for 10 minutes. The pellets of the AUM were washed twice with buffer A and proceeded to electron microscopy.

Purification of FimH-FimC complex

The cDNA of *fimH* and its chaperone *fimC* genes were cloned from *E. coli* DH5a into pACYCDuet-1 bicistronic plasmid (Sigma-Aldrich, Burlington, MA), and the resulting co-expression plasmid was introduced to *E coli.* BL21 (DE3) (Pellecchia et al., 1999). The bacteria were grown at 37℃ in LB medium containing chloramphenicol (34 µg/ml). At an OD600 of 0.7, IPTG was added to a final concentration of 0.5 mM. The cells were further grown for 18 hours at 15℃, harvested by centrifugation, washed by PBS, and disrupted by sonication. After removing cell debris by centrifugation, the supernatant was applied to Ni-NTA resin (Qiagen, Germantown, MD) and eluted with 20 mM Tris-HCl pH 8.0, 0.3 M imidazole. Fractions containing FimH-FimC were pooled and loaded onto a gel filtration column (ProteinArk, Rotherham, UK) equilibrated with 20 mM Hepes-NaOH pH 7.4, 150 mM NaCl. Fractions containing FimH-FimC were dialyzed against buffer A and were

concentrated using Vivaspin 2 (Sartorius, Göttingen, Germany). For cryo-EM, two times molar-excess FimH-FimC was mixed with the AUM (0.05 mg/ml) and incubated for 1 hour at 4℃ before plunge-freezing.

Cryo-electron microscopy of the AUM

The AUM was suspended in buffer A at a concentration of 0.05 mg/ml. 3 µl of the sample was applied to freshly glow-discharged holey carbon grids, Quantifoil R1.2/1.3 Cu/Rh 200 mesh (Quantifoil Micro Tools GmbH, Großlöbichau, Germany), blotted from both sides for 3 seconds at 4 ℃ under 99% humidity and plunge frozen in liquid ethane using Vitrobot Mark IV (Thermo Fisher Scientific, Waltham, MA). Images were recorded using a Titan Krios G4 microscope at the University of Tokyo (Thermo Fisher Scientific) at 300 keV, a Gatan Quantum-LS Energy Filter (Gatan, Pleasanton, CA) with a slit width of 20 eV, and a Gatan K3 BioQuantum direct electron detector in the electron counting mode. The nominal magnification was set to 64,000 × with a physical pixel size of 1.35 Å/pixel. Movies were acquired using the SerialEM software (Mastronarde, 2005), and the target defocus was set to 2.5-4.5 µm for tomography and 1-3 µm for single particle analysis (SPA). For tomography, each movie was recorded for 0.18 seconds with a total dose of 1.26 electrons/ $Å^2$ and subdivided into 10 frames. The angular range of the tilt series was from –60° to 60° with 3.0° increments using the dose-symmetric scheme (Hagen et al., 2017) or the continuous scheme. The total dose for one tilt series acquisition is thus 50 electrons $Å^2$. For SPA, each movie was recorded for 6.7 seconds with a total dose of 50 electrons/ $Å^2$ and subdivided into 50 frames. Specimens were tilted at 0, 30, 45, and 55°. The ratio of tilted images was 1:1:2:2 for 0, 30, 45, and 55°, respectively.

Data processing for tomography

Movies were subjected to beam-induced motion correction, image alignment, CTF correction, and reconstruction by back-projection using the IMOD software package (Kremer et al., 1996). Tomograms were 8 × binned and the centers of each uroplakin particle were manually selected using 3dmod tool. Volumes with 30-pixel^3 dimensions were extracted from 8 × binned tomograms and were averaged using the PEET software (Nicastro et al., 2006). A randomly selected subtomogram was used for the initial reference. Alignments were repeated twice for 8×binned and once for 4×binned tomograms with 60-pixel^3 dimensions. The averaged subtomogram was used for the reference in the subsequent SPA.

Data processing for SPA

Image processing was conducted using CryoSPARC v4.2.1 (Punjani et al., 2017) (Figure S1A). 4 × binned 128 pixel^2 images were picked and extracted from motion-corrected and CTF-corrected micrographs using the projections of the averaged subtomogram as references. The particle stack was cleaned by five rounds of 2D classification and three rounds of heterogeneous refinement. Following local motion correction and CTF refinement, homogenous refinement of unbinned 512 pixel^2 particles yielded a global resolution of 5 Å. At this point, the crystalline lipids were not observed. To increase the resolution, six uroplakin particles surrounding the central particle were subtracted, and the subsequent local refinement yielded a global resolution of 3.5 Å, visualizing the crystalline lipids. The edges of the AUM were often folded, which filled the distribution of orientations. However, the overlapping molecules compromised the precision of the side view alignment. The resolutions in the transverse and the vertical direction were calculated using the 3DFSC function of CryoSPARC.

Model building

The initial model was generated using AlphaFold-multimer (Jumper et al., 2021; Mirdita et al., 2022; Evans et al., 2022) and the *Sus scrofa* UPIa, UPIb, UPII, and UPIIIa sequences (Kwon et al., 2011; Visnjar et al., 2017). The AlphaFold-predicted model was refined using PHENIX (v.1.19.2-4158) real-space refinement tool with the secondary structure restraints and Ramachandran restraints on (Liebschner et al., 2019; Afonine et al., 2018). Carbohydrates were added to the Asn residues at the N-Glycosylation sites using Coot (v. 9.8.7) (Emsley et al., 2010; Emsley and Crispin, 2018). The models were further refined using UCSF Chimera, ChimeraX, and ISOLDE (Pettersen et al., 2004; Pettersen et al., 2021; Goddard et al., 2018; Croll, 2018). The refined model was validated using the comprehensive validation tool on PHENIX. Models of ceramide (CCD ID: 16C) and sphingosine (CCD ID: SPH) were fitted manually and refined using ISOLDE.

Lipidomic analysis

The lipid composition of the isolated AUM was analyzed using LC-MS. The total urothelium membrane homogenate was used as a control. Lipids were extracted by adding 2-propanol (50:1 by volume to control homogenate or 500 μL to AUM preparation). After centrifugation (10,000 ×g, 10 min, 4C), the supernatant was further diluted (1:10) by 2-propanol, and 3 μL was analyzed by LC-MS. The LC-MS system consisted of an Acquity UPLC system (Waters, Milford, MA), connected to an Exactive mass spectrometer equipped with a HESI-II ion source (Thermo Scientific, Waltham, MA). An Acquity UPLC BEH C8 column (1.0×100 mm, Waters) was used for reversed-phase chromatography with binary gradient elution with mobile phase A (10 mM ammonium formate in acetonitrile/water/formic acid (60/40/0.1)) and B (10 mM ammonium formate in 2-propanol/acetonitrile/water/formic acid (90/9.5/0.5/0.1)) at a flowrate of 100 μL/min. Following time program was used [time (%B)]: 0 min (30%) – 12 min (55%) – 18 min (70%) – 20 min (80%) – 22 min (99%) – 27 min

(99%) – 27.1 min (30%) – 28.5 min (30%). MS was operated in following conditions to perform data-independent, all-ions fragmentation (AIF) MS/MS acquisition: ionization polarity, positive and negative; scan range, 100-2,000 m/z; mass resolution, 25,000; maximum injection time, 500 ms; AGC target, balanced (1×10^6); in-source CID voltage, 0 V (off) and 35 V. MS-DIAL 4.9 software (Tsugawa et al., 2020). was used for peak detection, MS/MS deconvolution, alignment, integration, and lipid identification, of multiple samples. Lipid identification was based on searching lipid database provided with the software, with accurate mass tolerance of 0.005Da and 0.01Da for MS and MS/MS, respectively. For multiple candidates, those with highest score were adopted. No manual curation was performed for individual identifications, as the results were only used to estimate lipid classes abundant in AUM preparation. Peak intensities were normalized using built-in function of MS-DIAL, based on total signal for identified lipids (mTIC). R version 4.2 software was used for differential analysis using normalized peak intensity data exported from MS-DIAL. Fold enrichment values were calculated as a ratio for AUM versus control using triplicate, independently prepared samples.

Data availability

The map and the model will be available on the EMDB upon publication under the following accession numbers: EMD- 36340 , and PDB 8JJ5.

Acknowledgements

We thank Mrs. Natsuko Maruyama (University of Yamanashi) for technical assistance. This research is partially supported by Platform Project for Supporting Drug Discovery and Life Science Research (Basis for Supporting Innovative Drug Discovery and Life Science Research (BINDS)) from Japan Agency for Medical Research and Development (AMED)

under Grant Numbers JP22ama121002 and JP23ama121002 (support number 2639). This work was supported by the Takeda Science Foundation (to T.O.), the Daiichi Sankyo Foundation of Life Science (to T.O.), the Japan Society for the Promotion of Science (KAKENHI Grant numbers JP21H02654, JP22H05538 (T.O.), JP21H05248 (M.K.)), and the Naito Foundation (to T.O.). Molecular graphics and analyses performed with UCSF ChimeraX, developed by the Resource for Biocomputing, Visualization, and Informatics at the University of California, San Francisco, with support from National Institutes of Health R01-GM129325 and the Office of Cyber Infrastructure and Computational Biology, National Institute of Allergy and Infectious Diseases.

References

Hicks, R.M. 1965. The fine structure of the transitional epithelium of rat ureter. *J. Cell. Biol.* **26**, 25-48.

Hicks, R.M., Ketterer, B., and Warren, R.C. 1974. The ultrastructure and chemistry of the luminal plasma membrane of the mammalian urinary bladder: a structure with low permeability to water and ions. *Philos. Trans. R. Soc. Lond. B. Biol. Sci.* **268**, 23-38.

Frank, J., Goldfarb, W., Eisenberg, D., and Baker, T.S. 1978. Reconstruction of glutamine synthetase using computer averaging. *Ultramicroscopy*. **3**, 283-290.

Stubbs, C.D., Ketterer, B., and Hicks, R.M. 1979. The isolation and analysis of the luminal plasma membrane of calf urinary bladder epithelium. *Biochim. Biophys. Acta*. **558**, 58-72.

Radermacher, M. 1988. Three-dimensional reconstruction of single particles from random and nonrandom tilt series. *J. Electron. Microsc. Tech.* **9**, 359-394.

Hultgren, S.J., Abraham, S., Caparon, M., Falk, P., St, Geme JW 3rd, and Normark, S. 1993. Pilus and nonpilus bacterial adhesins: assembly and function in cell recognition. *Cell.* **73**,

887-901.

Lin, J.H., Wu, X.R., Kreibich, G., and Sun, T.T. 1994. Precursor sequence, processing, and urothelium-specific expression of a major 15-kDa protein subunit of asymmetric unit membrane. *J. Biol. Chem.* **269**, 1775-1784.

Yu, J., Lin, J.H., Wu, X.R., and Sun, T.T. 1994. Uroplakins Ia and Ib, two major differentiation products of bladder epithelium, belong to a family of four transmembrane domain (4TM) proteins. *J. Cell. Biol.* **125**, 171-182.

Walz, T., Häner, M., Wu, X.R., Henn, C., Engel, A., Sun, T.T., and Aebi, U. 1995. Towards the molecular architecture of the asymmetric unit membrane of the mammalian urinary bladder epithelium: a closed "twisted ribbon" structure. *J. Mol. Biol.* **248**, 887-900.

Wu, X.R., Medina, J.J., and Sun, T.T. 1995. Selective interactions of UPIa and UPIb, two members of the transmembrane 4 superfamily, with distinct single transmembrane-domained proteins in differentiated urothelial cells. *J. Biol. Chem.* **270**, 29752-29759.

Huang, H.W., Goldberg, E.M., and Zidovetzki, R. 1996. Ceramide induces structural defects into phosphatidylcholine bilayers and activates phospholipase A2. *Biochem. Biophys. Res. Commun.* **220**, 834-838.

Kremer, J.R., Mastronarde, D.N., and McIntosh, J.R. 1996. Computer visualization of three-dimensional image data using IMOD. *J. Struct. Biol.* **116**, 71-76.

Negrete, H.O., Lavelle, J.P., Berg, J., Lewis, S.A., and Zeidel, M.L. 1996. Permeability properties of the intact mammalian bladder epithelium. *Am. J. Physiol.* **271**, F886-894.

Hooton, T.M., and Stamm, W.E. 1997. Diagnosis and treatment of uncomplicated urinary tract infection. *Infect. Dis. Clin. North. Am.* **11**, 551-581.

Lavelle, J.P., Apodaca, G., Meyers, S.A., Ruiz, W.G., and Zeidel, M.L. 1998. Disruption of guinea pig urinary bladder permeability barrier in noninfectious cystitis. *Am. J. Physiol.* **274**, F205-214.

Liang, F., Kachar, B., Ding, M., Zhai, Z., Wu, X.R., and Sun, T.T. 1999. Urothelial hinge as a highly specialized membrane: detergent-insolubility, urohingin association, and in vitro formation. *Differentiation.* **65**, 59-69.

Pellecchia, M., Sebbel, P., Hermanns, U., Wüthrich, K., and Glockshuber, R. 1999. Pilus chaperone FimC-adhesin FimH interactions mapped by TROSY-NMR. *Nat. Struct. Biol.* **6**, 336-339.

Hu, P., Deng, F.M., Liang, F.X., Hu, C.M., Auerbach, A.B., Shapiro, E., Wu, X.R., Kachar, B., and Sun, T.T. 2000. Ablation of uroplakin III gene results in small urothelial plaques, urothelial leakage, and vesicoureteral reflux. *J. Cell. Biol.* **151**, 961-972.

Deng, F.M., Ding, M., Lavker, R.M., and Sun, T.T. 2001. Urothelial function reconsidered: a new role in urinary protein secretion. *Urology.* **57**, 117.

Grassme, H., Jekle, A., Riehle, A., Schwarz, H., Berger, J., Sandhoff, K., Kolesnick, R., and Gulbins, E. 2001. CD95 signaling via ceramide-rich membrane rafts. *J. Biol. Chem.* **276**, 20589-20596.

Grassme, H., Schwarz, H., and Gulbins, E. 2001. Molecular mechanisms of ceramide-mediated CD95 clustering. *Biochem. Biophys. Res. Commun.* **284**, 1016-1030.

Liang, F.X., Riedel, I., Deng, F.M., Zhou, G., Xu, C., Wu, X.R., Kong, X.P., Moll, R., and Sun, T.T. 2001. Organization of uroplakin subunits: transmembrane topology, pair formation and plaque composition. *Biochem. J.* **355**, 13-18.

Ulmschneider, M.B., and Sansom, M.S. 2001. Amino acid distributions in integral membrane protein structures. *Biochim. Biophys. Acta.* **1512**, 1-14.

Zhou, G., Mo, W.J., Sebbel, P., Min, G., Neubert, T.A., Glockshuber, R., Wu, X.R., Sun, T.T., and Kong, X.P. 2001. Uroplakin Ia is the urothelial receptor for uropathogenic Escherichia coli: evidence from in vitro FimH binding. *J. Cell. Sci.* **114**, 4095-4103.

Hu, P., Meyers, S., Liang, F.X., Deng, F.M., Kachar, B., Zeidel, M.L., and Sun, T.T. 2002.

Role of membrane proteins in permeability barrier function: uroplakin ablation elevates urothelial permeability. *Am. J. Physiol. Renal. Physiol.* **283**, F1200-1207.

Min, G., Stolz, M., Zhou, G., Liang, F., Sebbel, P., Stoffler, D., Glockshuber, R., Sun, T.T., Aebi, U., and Kong, X.P. 2002. Localization of uroplakin Ia, the urothelial receptor for bacterial adhesin FimH, on the six inner domains of the 16 nm urothelial plaque particle. *J. Mol. Biol.* **317**, 697-706.

Simons, K., and Ehehalt, R. 2002. Cholesterol, lipid rafts, and disease. *J. Clin. Invest.* **110**, 597-603.

Tu, L., Sun, T.T., and Kreibich, G. 2002. Specific heterodimer formation is a prerequisite for uroplakins to exit from the endoplasmic reticulum. *Mol. Biol. Cell.* **13**, 4221-4230.

Min, G., Zhou, G., Schapira, M., Sun, T.T., and Kong, X.P. 2003. Structural basis of urothelial permeability barrier function as revealed by Cryo-EM studies of the 16 nm uroplakin particle. *J. Cell. Sci.* **116**, 4087-4094.

Apodaca, G. 2004. The uroepithelium: not just a passive barrier. *Traffic.* **5**, 117-128.

Los, D.A., and Murata, N. 2004. Membrane fluidity and its roles in the perception of environmental signals. *Biochim. Biophys. Acta.* **1666**, 142-157.

Pettersen, E.F., Goddard, T.D., Huang, C.C., Couch, G.S., Greenblatt, D.M., Meng, E.C., and Ferrin, T.E. 2004. UCSF Chimera--a visualization system for exploratory research and analysis. *J. Comput. Chem.* **25**, 1605-1612.

Balogh, G., Horváth, I., Nagy, E., Hoyk, Z., Benkö, S., Bensaude, O., and Vígh, L. 2005. The hyperfluidization of mammalian cell membranes acts as a signal to initiate the heat shock protein response. *FEBS. J.* **272**, 6077-6086.

Hu, C.C., Liang, F.X., Zhou, G., Tu, L., Tang, C.H., Zhou, J., Kreibich, G., and Sun, T.T. 2005. Assembly of urothelial plaques: tetraspanin function in membrane protein trafficking. *Mol. Biol. Cell.* **16**, 3937-3950.

Mastronarde, D.N. 2005. Automated electron microscope tomography using robust prediction of specimen movements. *J. Struct. Biol.* **152**, 36-51.

Gensure, R.H., Zeidel, M.L., and Hill, W.G. 2006. Lipid raft components cholesterol and sphingomyelin increase H+/OH- permeability of phosphatidylcholine membranes. *Biochem. J.* **398**, 485-495.

Min, G., Wang, H., Sun, T.T., and Kong, X.P. 2006. Structural basis for tetraspanin functions as revealed by the cryo-EM structure of uroplakin complexes at 6-A resolution. *J. Cell. Biol.* **173**, 975-983.

Nicastro, D., Schwartz, C., Pierson, J., Gaudette, R., Porter, M.E., and McIntosh, J.R. 2006. The molecular architecture of axonemes revealed by cryoelectron tomography. *Science.* **313**, 944-948.

Xie, B., Zhou, G., Chan, S.Y., Shapiro, E., Kong, X.P., Wu, X.R., Sun, T.T., and Costello, C.E. 2006. Distinct glycan structures of uroplakins Ia and Ib: structural basis for the selective binding of FimH adhesin to uroplakin Ia. *J. Biol. Chem.* **281**, 14644-14653.

Jenkins, D., and Woolf, A.S. 2007. Uroplakins: new molecular players in the biology of urinary tract malformations. *Kidney. Int.* **71**, 195-200.

Khandelwal, P., Abraham, S.N., and Apodaca, G. 2009. Cell biology and physiology of the uroepithelium. *Am. J. Physiol. Renal. Physiol.* **297**, F1477-1501.

Thumbikat, P., Berry, R.E., Zhou, G., Billips, B.K., Yaggie, R.E., Zaichuk, T., Sun, T.T., Schaeffer, A.J., and Klumpp, D.J. 2009. Bacteria-induced uroplakin signaling mediates bladder response to infection. *PLoS. Pathog.* **5**, e1000415.

Wang, H., Min, G., Glockshuber, R., Sun, T.T., and Kong, X.P. 2009. Uropathogenic E. coli adhesin-induced host cell receptor conformational changes: implications in transmembrane signaling transduction. *J. Mol. Biol.* **392**, 352-361.

Wu, X.R., Kong, X.P., Pellicer, A., Kreibich, G., and Sun, T.T. 2009. Uroplakins in urothelial

biology, function, and disease. *Kidney. Int.* **75**, 1153-1165.

Emsley, P., Lohkamp, B., Scott, W.G., and Cowtan, K. 2010. Features and development of Coot. *Acta. Crystallogr. D. Biol. Crystallogr.* **66**, 486-501.

Kwon, D.N., Park, M.R., Park, J.Y., Cho, S.G., Park, C., Oh, J.W., Song, H., Kim, J.H., and Kim, J.H. 2011. Characterization of a putative cis-regulatory element that controls transcriptional activity of the pig uroplakin II gene promoter. *Biochem. Biophys. Res. Commun.* **410**, 264-269.

Lee, G. 2011. Uroplakins in the lower urinary tract. *Int. Neurourol. J.* **15**, 4-12.

Kanik-Prastowska, I., Lis, J., and Matejuk, A. 2014. Glycosylation of uroplakins. Implications for bladder physiopathology. *Glycoconj. J.* **31**, 623-636.

Lee, J.H., de, Val N., Lyumkis, D., and Ward, A.B. 2015. Model Building and Refinement of a Natively Glycosylated HIV-1 Env Protein by High-Resolution Cryoelectron Microscopy. *Structure.* **23**, 1943-1951.

Sodt, A.J., Pastor, R.W., and Lyman, E. 2015. Hexagonal Substructure and Hydrogen Bonding in Liquid-Ordered Phases Containing Palmitoyl Sphingomyelin. *Biophys. J.* **109**, 948-955.

Sorzano, C.O., Alcorlo, M., de, la Rosa- Trevín, J.M., Melero, R., Foche, I., Zaldívar-Peraza, A., del, Cano L., Vargas, J., Abrishami, V., Otón, J. et al. 2015. Cryo-EM and the elucidation of new macromolecular structures: Random Conical Tilt revisited. *Sci. Rep.* **5**, 14290.

Sauer, M.M., Jakob, R.P., Eras, J., Baday, S., Eriş, D, Navarra, G., Bernèche, S., Ernst, B., Maier, T., and Glockshuber, R. 2016. Catch-bond mechanism of the bacterial adhesin FimH. *Nat. Commun.* **7**, 10738.

Hagen, W.J.H., Wan, W., and Briggs, J.A.G. 2017. Implementation of a cryo-electron tomography tilt-scheme optimized for high resolution subtomogram averaging. *J. Struct. Biol.* **197**, 191-198.

Punjani, A., Rubinstein, J.L., Fleet, D.J., and Brubaker, M.A. 2017. cryoSPARC: algorithms for rapid unsupervised cryo-EM structure determination. *Nat. Methods.* **14**, 290-296.

Visnjar, T., Chesi, G., Iacobacci, S., Polishchuk, E., Resnik, N., Robenek, H., Kreft, M., Romih, R., Polishchuk, R., and Kreft, M.E. 2017. Uroplakin traffic through the Golgi apparatus induces its fragmentation: new insights from novel in vitro models. *Sci. Rep.* **7**, 12842.

Afonine, P.V., Poon, B.K., Read, R.J., Sobolev, O.V., Terwilliger, T.C., Urzhumtsev, A., and Adams, P.D. 2018. Real-space refinement in PHENIX for cryo-EM and crystallography. *Acta. Crystallogr. D. Struct. Biol.* **74**, 531-544.

Croll, T.I. 2018. ISOLDE: a physically realistic environment for model building into low-resolution electron-density maps. *Acta. Crystallogr. D. Struct. Biol.* **74**, 519-530.

Desai, A.J., and Miller, L.J. 2018. Changes in the plasma membrane in metabolic disease: impact of the membrane environment on G protein-coupled receptor structure and function. *Br. J. Pharmacol.* **175**, 4009-4025.

Emsley, P., and Crispin, M. 2018. Structural analysis of glycoproteins: building N-linked glycans with Coot. *Acta. Crystallogr. D. Struct. Biol.* **74**, 256-263.

Goddard, T.D., Huang, C.C., Meng, E.C., Pettersen, E.F., Couch, G.S., Morris, J.H., and Ferrin, T.E. 2018. UCSF ChimeraX: Meeting modern challenges in visualization and analysis. *Protein. Sci.* **27**, 14-25.

Ghysels, A., Krämer, A., Venable, R.M., Teague, W.E. Jr, Lyman, E., Gawrisch, K., and Pastor, R.W. 2019. Permeability of membranes in the liquid ordered and liquid disordered phases. *Nat. Commun.* **10**, 5616.

Liebschner, D., Afonine, P.V., Baker, M.L., Bunkóczi, G., Chen, V.B., Croll, T.I., Hintze, B., Hung, L.W., Jain, S., McCoy, A.J. et al. 2019. Macromolecular structure determination using X-rays, neutrons and electrons: recent developments in Phenix. *Acta. Crystallogr. D. Struct.*

Biol. **75**, 861-877.

Righetto, R.D., Biyani, N., Kowal, J., Chami, M., and Stahlberg, H. 2019. Retrieving high-resolution information from disordered 2D crystals by single-particle cryo-EM. *Nat. Commun.* **10**, 1722.

Kusumi, A., Fujiwara, T.K., Tsunoyama, T.A., Kasai, R.S., Liu, A.A., Hirosawa, K.M., Kinoshita, M., Matsumori, N., Komura, N., Ando, H. et al. 2020. Defining raft domains in the plasma membrane. *Traffic.* **21**, 106-137.

Ord, M., Faustova, I., and Loog, M. 2020. The sequence at Spike S1/S2 site enables cleavage by furin and phospho-regulation in SARS-CoV2 but not in SARS-CoV1 or MERS-CoV. *Sci. Rep*. **10**, 16944.

Tsugawa, H., Ikeda, K., Takahashi, M., Satoh, A., Mori, Y., Uchino, H., Okahashi, N., Yamada, Y., Tada, I., Bonini, P. et al. 2020. A lipidome atlas in MS-DIAL 4. *Nat. Biotechnol.* **38**, 1159-1163.

Johnson, B.A., Xie, X., Bailey, A.L., Kalveram, B., Lokugamage, K.G., Muruato, A., Zou, J., Zhang, X., Juelich, T., Smith, J.K. et al. 2021. Loss of furin cleavage site attenuates SARS-CoV-2 pathogenesis. *Nature*. **591**, 293-299.

Jumper, J., Evans, R., Pritzel, A., Green, T., Figurnov, M., Ronneberger, O., Tunyasuvunakool, K., Bates, R., Žídek, A., Potapenko, A. et al. 2021. Highly accurate protein structure prediction with AlphaFold. *Nature*. **596**, 583-589.

Pettersen, E.F., Goddard, T.D., Huang, C.C., Meng, E.C., Couch, G.S., Croll, T.I., Morris, J.H., and Ferrin, T.E. 2021. UCSF ChimeraX: Structure visualization for researchers, educators, and developers. *Protein. Sci*. **30**, 70-82.

Prestegard, J.H. 2021. A perspective on the PDB's impact on the field of glycobiology. *J. Biol. Chem.* **296**, 100556.

Zhang, T., Hu, W., and Chen, W. 2021. Plasma Membrane Integrates Biophysical and

Biochemical Regulation to Trigger Immune Receptor Functions. *Front. Immunol.* **12**, 613185.

Zhao, P., Zhao, C., Chen, D., Yun, C., Li, H., and Bai, L. 2021. Structure and activation mechanism of the hexameric plasma membrane H(+)-ATPase. *Nat. Commun.* **12**, 6439.

El, Mazouni D., and Gros, P. 2022. Cryo-EM structures of peripherin-2 and ROM1 suggest multiple roles in photoreceptor membrane morphogenesis. *Sci. Adv.* **8**, eadd3677.

Evans, R., O'Neill, M., Pritzel, A., Antropova, N., Senior, A., Green, T., Zidek, A., Bates, R., Blackwell, S., Yim, J. et al. 2022. Protein complex prediction with AlphaFold-Multimer. *bioRxiv.* **DOI**, 10.1101/2021.10.04.463034.

Mirdita, M., Schütze, K., Moriwaki, Y., Heo, L., Ovchinnikov, S., and Steinegger, M. 2022. ColabFold: making protein folding accessible to all. *Nat. Methods.* **19**, 679-682.

Oda, T., Yanagisawa, H., Shinmori, H., Ogawa, Y., and Kawamura, T. 2022. Cryo-electron tomography of Birbeck granules reveals the molecular mechanism of langerin lattice formation. *Elife.* **11***:* e79990.

Watanabe, T., Suzuki, A., Ohira, S., Go, S., Ishizuka, Y., Moriya, T., Miyaji, Y., Nakatsuka, T., Hirata, K., Nagai, A. et al. 2022. The Urinary Bladder is Rich in Glycosphingolipids Composed of Phytoceramides. *J. Lipid. Res.* **63**, 100303.

Dutka, P., Metskas, L.A., Hurt, R.C., Chou, T., Shapiro, M.G., and Jensen, G.J. 2023. Structure of Anabaena flos-aquae gas vesicles revealed by cryo-ET. *Biophys. J.* **122**, 40A.

Figure Legends

Figure 1: Cryo-electron microscopy of the AUM. (A) Representative micrographs of the AUM. Tilt angles are indicated. (B) 2D class averages of the particles. (C) Reconstructed hexagonal array of the uroplakin complex. (D) Local refinement of the central uroplakin complex. Top and side views are shown. Hexagonally-aligned crystalline lipids are visualized.

Figure 2: Models of the uroplakin complex and the crystalline lipids. (A, B) Models of the hexameric complex (A) and single heterotetramer (B) are shown. An initial model was predicted using AlphaFold and real-space refined using PHENIX and ISOLDE. Lipid models (C16 ceramide or sphingosine) were manually fitted and refined using ISOLDE. Purple: UPIa; cyan: UPIb; pink: UPII; green: UPIIIa; and yellow: lipids. (B) Residues magnified in C are indicated. (C) Possible interactions between the side chains and the lipid head groups were indicated. (D) Beta-sheet of UPII with discernible side-chains.

Figure 3: Interactions between the UPIa/Ib transmembrane helices and the lipids. Vertically-aligned bulky side chains appear to be incorporated into the crystalline lipids. Top (left) and side (right) views are shown.

Figure 4: Glycosylation of the uroplakin subunits. Six N-glycosylation sites were visualized in the reconstruction. The large densities of the carbohydrate chains at Asn139 of UPIIIa may interact with the N-terminal loop of the adjacent IIIa. Asn19 of UPII, which was also predicted to be glycosylated (Hu et al., 2005), was not observed in our map, probably due to the cleavage of the N-terminal signal sequence.

Figure 5: UPIa-Ib interface. (A) The interface between UPIa and Ib is characterized by two opposing helices (broken circles). Top views (A, C, and D, right) are shown. (B) Hydrophobic interaction between UPIa F196 and Ib L155 (arrowhead). (C and D) Hydrogen bonds between UPIa D150 - Ib K197, Ia R147 - Ib D157, and Ia N195 - Ib Q130 are indicated (arrowheads). The bond between Ia R147 - Ib D157 is less reliable due to its weak densities. (D) The electron densities of the hydrogen bonds are shown in mesh. Distances are indicated.

Figure 6: **UPII-IIIa, IIIa-IIIa, and the intra-membrane interfaces.** (A) Hydrophobic interaction between UPII and IIIa. Disulfide bonds between Cys51-Cys80 of UPII and between Cys47-Cys110 of IIIa are facing each other, and the interface appears to be supported by Pro79 of UPII and Leu113 of IIIa. (B) IIIa-IIIa interface. Pro164 at the apex of the loop 137-161 of IIIa (arrows) inserts into the groove of Leu66 and Trp182 of the adjacent IIIa. (C) The interface between the transmembrane helices of Ia and Ib. At the pseudo-symmetric center of Ia and Ib (broken circle, right), a cluster of hydrophobic side chains mediates the Ia-Ib interaction.

Figure 7: **Lipidomic analysis of the AUM.** The chart displays the fold-enrichment of each lipid species detected in the sarkosyl-insoluble AUM fraction relative to the whole bladder scrape. Lipids were extracted from both sample types and analyzed using liquid chromatography-mass spectrometry (LC-MS). The peak heights were normalized by dividing them by the total signal for all identified lipids for each experiment. The fold-enrichment values indicate the difference in relative abundance of each lipid species in the sarkosyl-insoluble AUM fraction compared to the whole bladder scrape, with higher values suggesting an enrichment in the AUM fraction. The result for positive ion mode is shown. Data represent

the mean fold-enrichment and standard deviation from three independent experiments (n = 3).

Supplemental Materials

Supplemental Figures 1-3

Supplemental Table 1

Supplemental Spread sheet 1

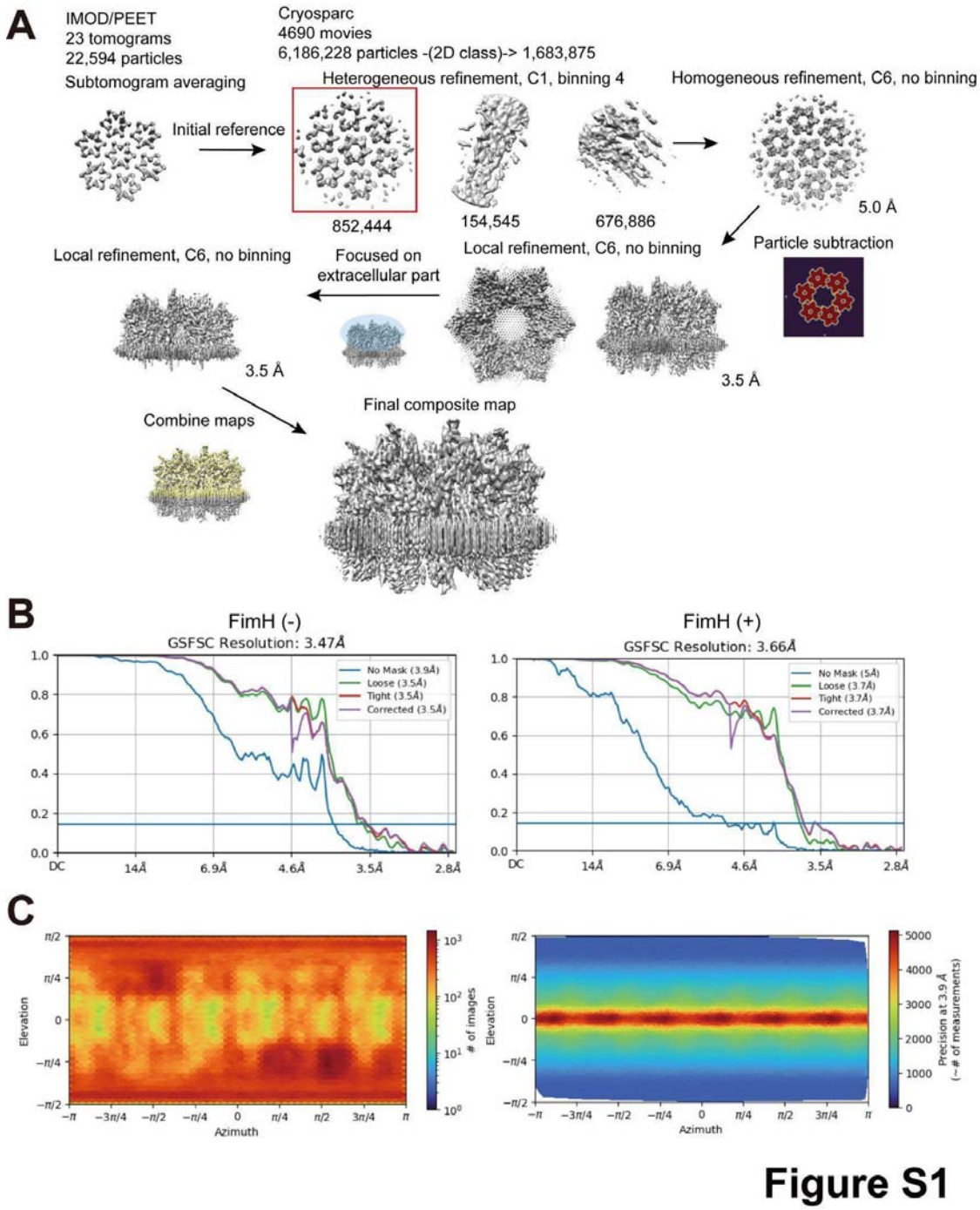

Figure S1

Supplementary Figure 1: Cryo-electron microscopy of the AUM. (A) Summary of the reconstruction procedure. (B) Resolution estimations using Fourier shell correlation. The cut-off value is 0.143. The left and right curves are without and with FimH, respectively. (C) The viewing direction distribution (left) and the posterior precision directional distribution (right). Although the distribution of the views covers nearly entire directions, the precision of the

side views deteriorates due to the overlapping molecules.

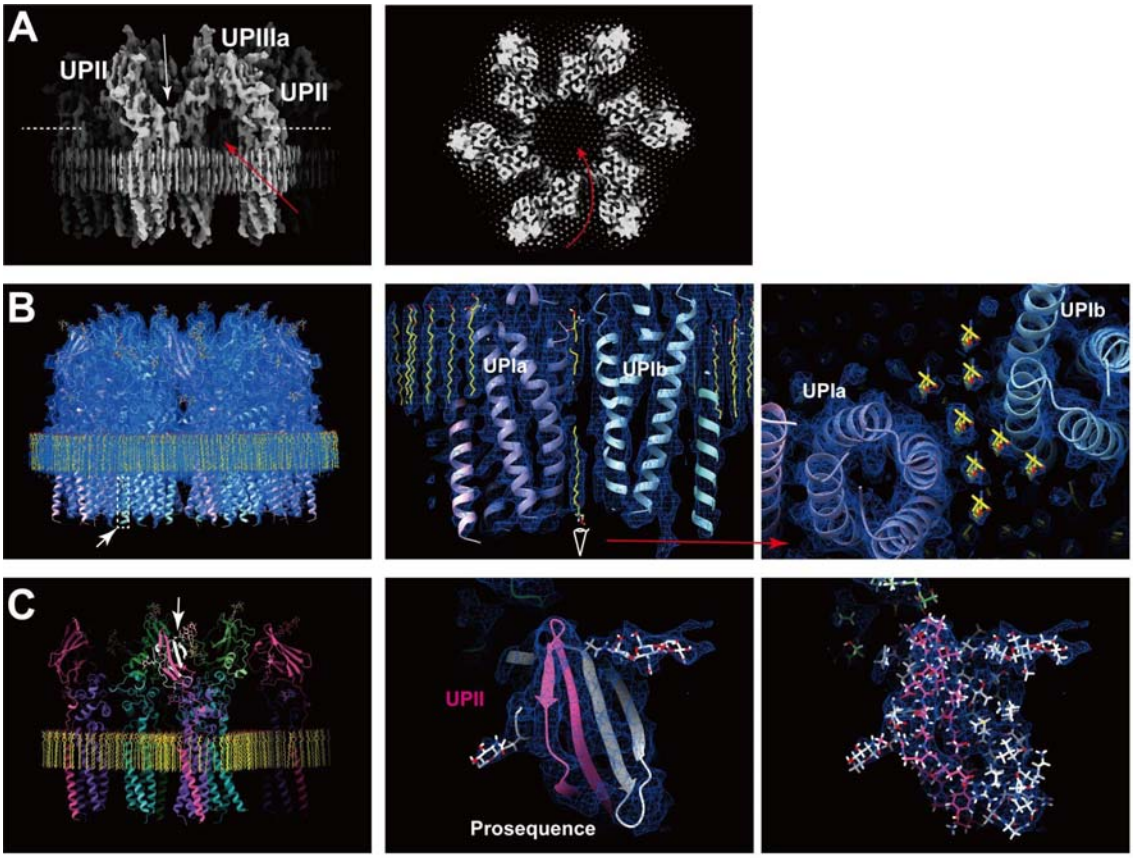

Figure S2

Supplementary Figure 2: Additional structural features. (A) Y-shaped conformation of the uroplakin heterotetramer. The white and red arrows indicate the groove between UPII and UPIIIa, and the channel beneath the II-IIIa arch, respectively. The broken lines indicate the position of the cross-section on the right panal. (B) Weak signals of lipids of the inner leaflet (arrow). The view from the cytoplasmic side (right) shows the hexagonal alignment of the inner lipids (yellow). (C) The prosequence of UPII (arrow, models in white) forms an anti-parallel beta-sheet structure. The electron densities (mesh) validate the assignment of the domain (middle and right).

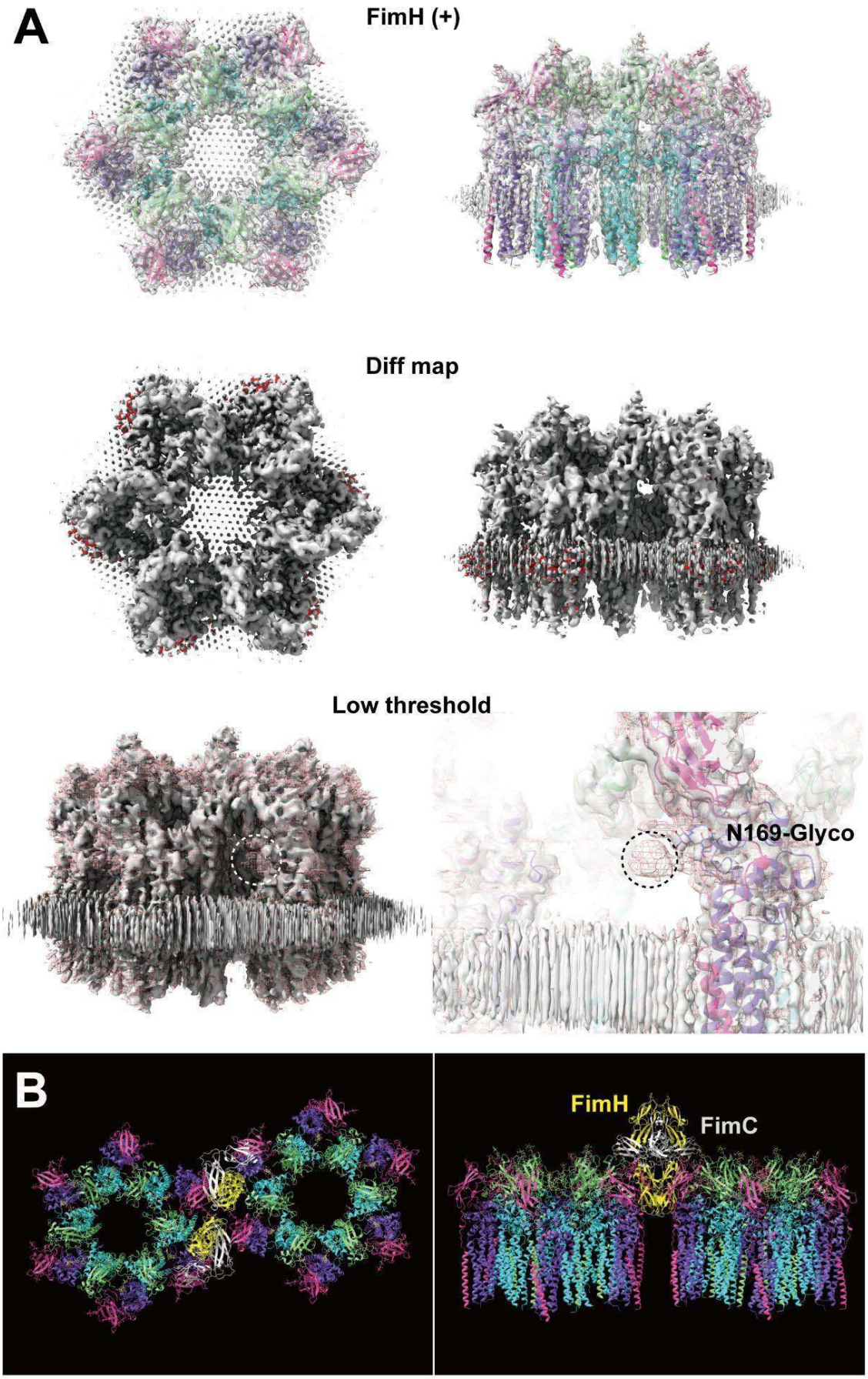

Figure S3

Supplementary Figure 3: FimH-bound uroplakin structure. (A) Uroplakin structure in the presence of FimH-FimC complexes. Model fitting (top) and the difference map (middle) indicate no conformational changes within the uroplakin complex. The difference map shows scattered signals in the lipid regions near the Ia/II heterodimer, suggesting an altered lipid configuration. (B) Model of the uroplakin complex pair with bound FimH-FimC complexes (PDBID: 1QUN). The gap between the two neighboring uroplakin complexes is so narrow that the mannose-binding domain of FimH barely fits.

Supplementary Table 1: Summary of data collection and model validation

Data collection parameters	
Magnification	64,000×
Pixel size (Å)	1.35
Voltage (keV)	300
	Tomography
Defocus range (µm)	2.5-4.5
Exposure time (sec/tilt)	0.18
Number of frames per tilt	10
Angular range (°)	±60
Increments (°)	3
Total dose ($e^-/Å^2$)	50
Number of tilt series recorded	95

Number of tilt series processed	23
Initial number of subtomograms	83,109
Final number of subtomograms	22,594
	SPA
Defocus range (µm)	1.1-4.5
Exposure time (sec)	6.7
Number of frames	50
Total dose ($e^-/Å^2$)	50
Tilt angles (°)	0, 30 , 45, 55
Ratio of tilted images	1:1:2:2 for 0, 30, 45, 55°
Number of movies recorded	4,690 (FimH-)/2,733 (FimH+)
Box size (pixels)	512
Initially picked particles	12,764,463 (FimH-)/6,619,664 (FimH+)
Final particles	609,567 (FimH-)/177,303 (FimH+)
Model validation statistics	
Initial model used	AlphaFold prediction
Bonds length RSMD (Å)	0.023
Bonds angles RSMD (°)	2.466
MolProbability score	1.74

Clash score	2.55
Rotamer outliers (%)	1.49
Ramachandran plot (%)	Favored: 89.25 Allowed: 10.75 Outliers: 0.00
CaBLAM outliers (%)	4.37
B-factors (min/max/mean)	59.32/134.09/93.14
Map resolution estimates (Å)	3.5 ($FSC_{half\text{-}map}$=0.143) 3.6 (FSC_{model}=0.143)

Supplemental spread sheet 1: Numerical data used for generating boxplot in Figure 7.